

# Hot Deformation Behavior of Near- $\alpha$ Titanium Alloy Ti-1100 Prepared by TiH<sub>2</sub>-based Powder Metallurgy

Piao Rongxun<sup>1,2</sup>, Yang Shaoli<sup>1,2</sup>, Zhu Yuling<sup>3</sup>, Ma Lan<sup>1,2</sup>

<sup>1</sup> Panzhihua University, Panzhihua 617000, China; <sup>2</sup> Sichuan Key Laboratory of Comprehensive Utilization of Vanadium and Titanium Resources, Panzhihua 617000, China; <sup>3</sup> Xihua University, Chengdu 610039, China

**Abstract:** Hot deformation behavior of TiH<sub>2</sub>-based powder metallurgy (PM) near- $\alpha$  titanium alloy Ti-1100 alloys was investigated in temperature range of 973–1173 K and strain rate range of 0.01–1.0 s<sup>-1</sup> by hot compression tests. The Arrhenius constitutive equation was developed and the hot deformation activation energy was calculated to be 334.76 kJ/mol. The temperature sensitivity ( $\theta$ ) was calculated by a modified function and the strain rate sensitivity ( $m$ ) was determined. Based on the results of temperature sensitivity and strain rate sensitivity together with microstructure at strain of 0.5, the hot working condition was analyzed. Results show that the instability regions mainly appear at strain rate of 0.01 and 1 s<sup>-1</sup> over whole temperature range, while the optimal hot working conditions are obtained in the range of 1135 K/0.29 s<sup>-1</sup> to 1173 K/0.76 s<sup>-1</sup>, and 1040 K/0.33 s<sup>-1</sup> to 1096 K/0.6 s<sup>-1</sup>. Besides, the dynamic recrystallization (DRX) occurs at strain rate of 0.01–0.1 s<sup>-1</sup>, and the formation of micro-voids is the dominant mechanism of flow softening at strain rate of 1 s<sup>-1</sup>.

**Key words:** Ti-1100 alloy; TiH<sub>2</sub>-based powder metallurgy; hot compression test; Arrhenius constitutive model; strain rate sensitivity; temperature sensitivity; hot workability

Near- $\alpha$  titanium alloys known to have high temperature properties and superior to  $\alpha+\beta$  type titanium alloys are the best choices for their high strength-to-weight ratio, good corrosion resistance, and higher temperature capability among various materials, which are candidates in high-temperature applications as compressor of turbojet engines<sup>[1]</sup>. Ti-1100 (Ti-6Al-2.75Sn-4Zr-0.4Mo-0.4Si, wt%) has the highest capability to tolerate temperature up to 873 K without any degradation in mechanical properties among near- $\alpha$  titanium alloys<sup>[2,3]</sup>. However, like most titanium alloys, the high manufacturing cost associated with expensive raw materials and processing difficulties has been always the main key issue for wide commercial applications<sup>[4]</sup>. The blended elemental powder metallurgy (PM) is one of the most promising methods for production of titanium alloy components with low cost<sup>[4-6]</sup>. However, compared with ingot metallurgy (IM) titanium alloys, challenge of PM ones has high oxygen contamination and insufficiently high density<sup>[7]</sup>. Ductility

always decreases dramatically as the oxygen content exceeds 0.35 wt%<sup>[8]</sup>.

Over the past several years, it has been demonstrated that PM parts developed using TiH<sub>2</sub> powder feedstock instead of titanium powder or hydride-dehydride (HDH) titanium powder achieve near-theoretical densities, and have better control over lower oxygen content, microstructures, and good chemical homogeneity<sup>[7,9-11]</sup>. The brittleness of Ti hydride results in a tendency of the powder to crush easily during the cold isostatic pressing (CIP), so high as-sintered density can be easily achieved. During the sintering in vacuum, the decomposition of hydride above 400 °C causes the development of high density of crystal lattice defects, resulting in the acceleration of sintering, easier diffusion of alloy elements by reducing activation energy, and reduction of oxygen by nascent hydrogen, which thus helps to develop fine-grained microstructure along with high density<sup>[9,10,12]</sup>. More details of the mechanism of sintering and densification

Received date: May 12, 2020

Foundation item: Panzhihua Science and Technology Program (2018CY-G-3); "Seed fund" Project of Science Park of Panzhihua University (Science Park 2019-05)  
Corresponding author: Ma Lan, Master, Professor, Department of Vanadium and Titanium, Panzhihua University, Panzhihua 617000, P. R. China, Tel: 0086-812-3372090, E-mail: hudie5656@163.com

Copyright © 2020, Northwest Institute for Nonferrous Metal Research. Published by Science Press. All rights reserved.

have been found in Ref.[9-13]. Using  $\text{TiH}_2$  powder, a density larger than 95% can be easily obtained, so this process can eliminate the costly hot isostatic pressing (HIP) operation applied to PM parts that are produced conventionally<sup>[12]</sup>. It can be found that many kinds of PM parts, mainly  $\alpha+\beta$  titanium alloys such as TC4, have been explored by this process<sup>[5,12,14]</sup>. But few study has been reported on near  $\alpha$  titanium alloy, especially Ti-1100 alloy. So far, Hagiwara et al<sup>[4]</sup> have reported the blended elemental (BE) PM synthesis of Ti-1100 alloy using extra low chlorine (ELCL) hydride-dehydride (HDH) titanium powder and master alloy powder. They concluded that the density of PM synthesis of alloy reaches 95% of theoretical density, and the conventional BE PM of cold pressing-vacuum sintering-hot isostatic pressing (HIP) produces a fine grain-size (150  $\mu\text{m}$  in diameter) colony microstructure, whereas the new BE PM method, in which a heat treatment step is added prior to final HIP, produces a fine grain-size acicular microstructure, resulting in better performance in tensile strength and high cycle fatigue strength. Very recently, Niu et al<sup>[7]</sup> studied the microstructures and mechanical behavior of near  $\alpha$  Ti-3Al-2Zr-2Mo titanium alloy prepared by  $\text{TiH}_2$ -based powder metallurgy. Through a series of cold pressing-sintering-hot extrusion process followed by both vacuum annealing and common annealing, satisfying combination of superior tensile strength and excellent ductility can be obtained.

Traditionally, a series of hot working and heat treatment steps are usually performed on melted ingot or PM alloy to refine the microstructure<sup>[5]</sup>. In order to achieve the optimal hot working condition with refined microstructure, it is essential to study the hot deformation behavior of the materials. Several researches have been studied on the constitutive models, processing maps and microstructure evolution of some near  $\alpha$  titanium alloys. For example, Krishna et al<sup>[15]</sup> investigated the hot deformation mechanism in near- $\alpha$  titanium alloy 685 by constructing processing map, obtained the optimal condition of 975 °C and 0.001  $\text{s}^{-1}$  and proposed that dynamic recrystallization (DRX) occurs due to low oxygen level in the alloy. Zhou et al<sup>[16]</sup> studied hot workability of near- $\alpha$  titanium alloy Ti-6Al-3Nb-2Zr-1Mo with an initial duplex microstructure through isothermal compression. By integrating process maps and constitutive relationship, they proposed that the optimal hot working domain appears under condition of 925~975 °C/0.01~0.1  $\text{s}^{-1}$ , and the main mechanism of microstructure evolution in  $\alpha+\beta$  phase field is super-plasticity deformation (SPD) and dynamic recrystallization (DRX) of  $\beta$  phase. Balasundar et al<sup>[17]</sup> deeply discussed geometric dynamic recrystallization behavior of a near- $\alpha$  titanium alloy TTTAN 29A (equivalent to IMI834) with acicular microstructure through hot compression tests over a temperature range of 850~1060 °C and strain rate range of  $3\times 10^{-4}$ ~1  $\text{s}^{-1}$ , and proposed the optimum condition of 920~1030 °C at low strain rates of  $3\times 10^{-4}$ ~ $10^{-3}$   $\text{s}^{-1}$ , by which geometric dynamic recrystal-

lization (DRX) or spheroidization of  $\alpha$  lamellae is dominant mechanism of microstructure evolution. All these studies have been focused on as-cast alloy. However, the study of hot deformation behavior for PM alloy is rarely reported at present. In hot deformation investigation, the constitutive relationships of alloys during hot deformation were generally studied by the Arrhenius constitutive model<sup>[18-20]</sup>. The hot workability of alloys was often determined based on strain rate sensitivity<sup>[21-24]</sup>. In addition, as an alloy with low thermal conductivity, titanium alloy during hot deformation is not only sensitive to strain rate, but also to temperature. Therefore, discussing the effect of strain rate sensitivity and temperature sensitivity on hot deformation behavior is of great importance.

This study aimed to investigate the hot deformation behavior of  $\text{TiH}_2$ -based PM near- $\alpha$  Ti-1100 titanium alloy through hot compression tests in temperature range of 973~1173 K and strain rate range of 0.01~1.0  $\text{s}^{-1}$ . To understand the hot deformation behavior, the constitutive relationship, temperature sensitivity and strain rate sensitivity were investigated. The deformed microstructures were observed by optical microscopy (OM) and scanning electron microscopy (SEM). The results will provide guidance for optimizing hot processing routes and developing high performance Ti-1100 alloys by  $\text{TiH}_2$ -based PM.

## 1 Experiment

Titanium hydride powder (Ti-4.5H-0.12O-0.015C-0.023N-0.016Fe, wt%) with a particle size of 45  $\mu\text{m}$  was used as raw materials in the experiments. The high grade of pure alloying elements Al, Sn, Zr, Mo, and Si were added at mass ratio of 6.5:4:2.7:0.4:0.4 and well mixed by the ball-mill machine. After mixing, the mixture was put into the soft rubber mold with cylindrical shape ( $\Phi 35$  mm $\times$ 120 mm) and subjected to cold isostatic press under the pressure of 240 MPa for 180 s. Then sintering was carried out in a vacuum sintering furnace. Before heating, the vacuum in the furnace was adjusted to  $5\times 10^{-3}$  Pa by mechanical and molecular pump, and heating was started. When the temperature reached 1150 °C, the Ar gas was injected to maintain chamber pressure of 80~120 Pa, and then the specimen was sintered for 4 h followed by furnace cooling. The X-ray diffraction (XRD) pattern and back-scattering electron (BSE) image of initial microstructure of the as-sintered alloys are shown in Fig.1. It shows that the alloys are typical two-phase microstructure, mainly consist of lath  $\alpha$  phase with a length of 30  $\mu\text{m}$  and a width of 10~20  $\mu\text{m}$ , and  $\beta$  phase in the  $\alpha$  phase boundary. From preliminary density measurements<sup>[25]</sup>, the density of as-sintered alloy was determined to be 95.45% of the theoretical density and the chemical composition of sintered alloy is shown in Table 1.

Cylindrical specimens with the size of  $\Phi 8$  mm $\times$ 12 mm were spark-machined from the sintered billets with their cylinder axis parallel to the hot pressing direction. Hot compression tests were carried out on a THERMECMMASTER-Zthermos-simulation

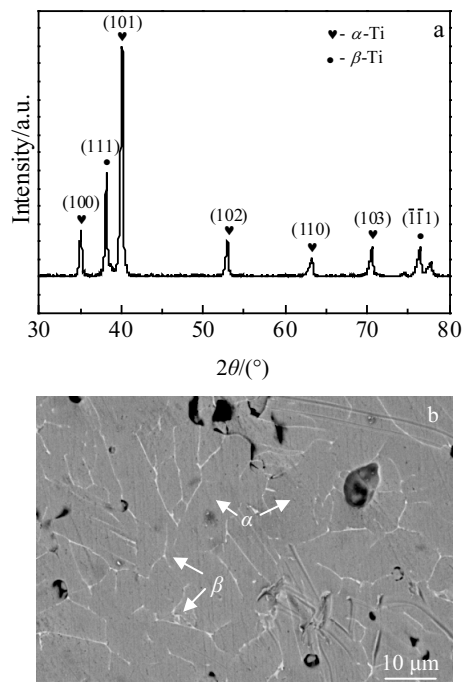


Fig.1 XRD pattern (a) and BSE image (b) of as-sintered alloy

**Table 1 Chemical composition of sintered alloy (wt%)**

Ti	Al	Zr	Sn	Mo	Si	C	N	H	O
88.3	5.05	3.689	1.96	0.32	0.29	0.0071	0.0013	0.0016	0.12

machine at temperatures of 973~1173 K with an interval of 50 K and strain rates of 0.01, 0.1 and 1.0  $s^{-1}$  under the vacuum degree lower than 10 Pa. The specimens were heated up to the deformed temperature with the rate of 10 K/s, and kept for 180 s to ensure uniformed temperature distribution. The height reduction during hot compression was 50% for specimens under all deformation conditions. It should be noticed that the 0.1 mm thick mica wafer was used on both end faces between the specimens and die to minimize interface friction. The true stress-strain curves were acquired automatically by a computer-equipped monitor. After deformation, the specimens were quickly cooled down to room temperature by Ar gas with a cooling rate of about 20 K/s up to 773 K. The isothermally compressed specimens were cut along the radial direction parallel to the compression axis, and then they were prepared for microstructure observation by metallographic preparation processes.

## 2 Results and Discussion

### 2.1 Flow stress curves

Fig.2 shows the macro-appearance of deformed samples under different processing conditions. It can be seen that the shear failure with crack angle  $45^\circ$  on the surface is observed in the sample deformed at temperature of 973 K and strain rate

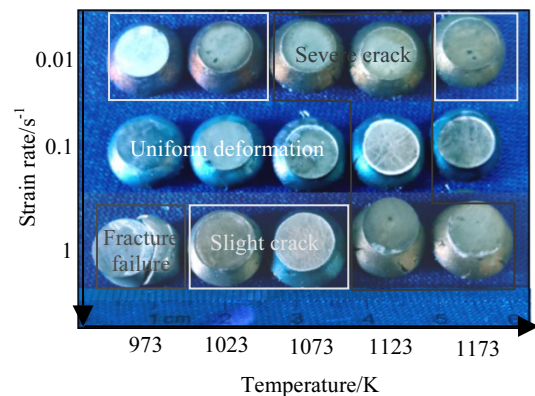


Fig.2 Macro-appearance of deformed alloys under different processing conditions

of 1  $s^{-1}$ . Also, severe macro-crack or slight crack are observed mainly in the samples deformed at temperature of 973~1173 K and strain rate of 0.01  $s^{-1}$ , as well as temperature of 1023~1173 K and strain rate of 1  $s^{-1}$ . However, no obvious macro-crack is observed at medium strain rate of 0.1  $s^{-1}$  and temperature from 973 K to 1173 K except the condition at 1123 K and 0.1  $s^{-1}$ .

The true stress-strain curves under different deformation conditions are shown in Fig.3. It shows a typical phenomenon that the true stress rises with decreasing the deformation temperature and increasing the strain rate. In the early deformation stage, the flow stress increases rapidly to a peak stress, due to work hardening effect caused by the increase of dislocation<sup>[26]</sup>. After a sharp increase, the flow stress decreases with increasing the strain due to dynamic softening effects, such as dynamic recovery (DRV) or dynamic recrystallization (DRX)<sup>[17,27-29]</sup>. Eventually, the softening and work hardening effects reach a dynamic balance, resulting in a flow-stress plateau. This plateau is more obvious at high deformation temperature and high strain rate. In case of samples deformed under 1173 K/0.1  $s^{-1}$  and 1023 K/1  $s^{-1}$ , as shown in Fig.3b and 3c, the true stress tends to increase with the further increase of strain, implying that the hardening effect becomes dominant by microstructure evolution.

### 2.2 Constitutive relationship

In order to understand the relationships between the true stress and the deformation parameters such as temperature, strain and strain rate, the well-known Arrhenius constitutive equation<sup>[18]</sup> is introduced. This model is usually expressed by the following three equations<sup>[19,20]</sup>.

$$\dot{\epsilon} = A_1 \sigma_p^n \exp(-Q/RT) \quad (1)$$

$$\dot{\epsilon} = A_2 \exp(\beta \sigma_p) \exp(-Q/RT) \quad (2)$$

$$\dot{\epsilon} = A[\sinh(\alpha \sigma_p)]^n \exp(-Q/RT) \quad (3)$$

where  $\dot{\epsilon}$  is strain rate ( $s^{-1}$ ),  $Q$  is the deformation activation energy ( $kJ \cdot mol^{-1}$ ),  $R$  is gas constant ( $R=8.314 J \cdot mol^{-1} \cdot K^{-1}$ ),  $T$  is absolute temperature (K),  $\sigma_p$  is peak stress, the rests are material constants, and  $\alpha=\beta/n$ . Eq.(1) and Eq.(2) are suitable

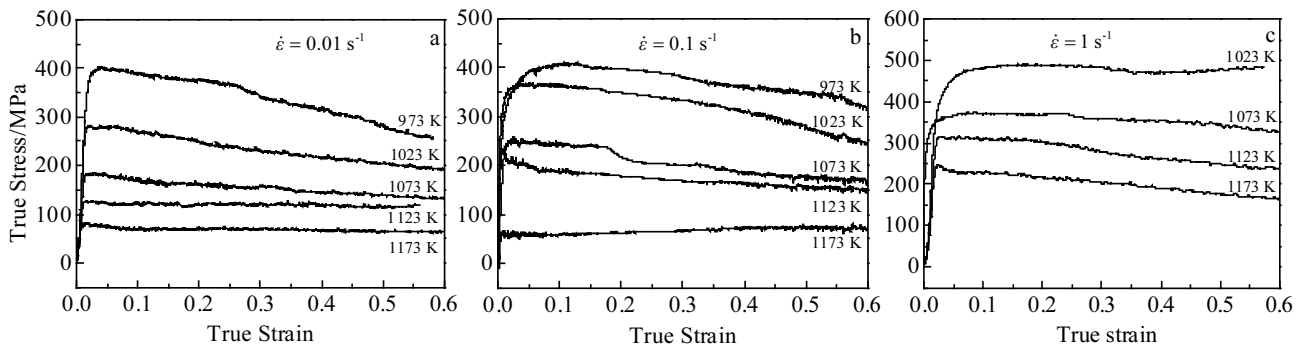


Fig.3 True stress-strain curves of Ti-1100 alloy under different deformation conditions: (a) 0.01 s<sup>-1</sup>, (b) 0.1 s<sup>-1</sup>, and (c) 1 s<sup>-1</sup>

for low stress range ( $\alpha\sigma < 0.8$ ) and high stress range ( $\alpha\sigma > 1.2$ ) respectively, while Eq.(3) is suitable for all conditions. Thus the hyperbolic-sine law Eq.(3) is generally used to explain the deformation behavior over a wide range of stresses.

Taking natural logarithm for Eq.(1~3), Eq.(4~6) are obtained.

$$\ln \dot{\epsilon} = \ln A_1 + n' \ln \sigma_p - Q/RT \quad (4)$$

$$\ln \dot{\epsilon} = \ln A_2 + \beta \sigma_p - Q/RT \quad (5)$$

$$\dot{\epsilon} = \ln A + n [\ln \sinh(\alpha \sigma_p)] - Q/RT \quad (6)$$

According to Eq.(4) and Eq.(5), the material constants of  $n'$  and  $\beta$  can be determined to be 5.90 and 0.0233 by calculating the average values of the slopes of the  $\ln \sigma_p - \ln \dot{\epsilon}$  and  $\sigma_p - \ln \dot{\epsilon}$  curves, as shown in Fig.4a and 4b, respectively. Subsequently, the value of  $\alpha$  in constitutive Eq.(6) is calculated to be 0.0044 MPa<sup>-1</sup>.

According to Eq.(6), the values of  $n$  and  $Q$  can be determined to be 4.013 and 334.76 kJ/mol by calculating the average slopes of linear fitting curves of  $\ln[\sinh(\alpha \sigma_p)] - \ln \dot{\epsilon}$  and  $\ln[\sinh(\alpha \sigma_p)] - 1/T$ , as shown in Fig.4c and 4d. The  $Q$  value determined in present study is much higher than the self-diffusion activation energy of  $\alpha$  phase (150 kJ/mol) or that of  $\beta$  phase (153 kJ/mol), and this result is consistent with the general view that a higher activation energy is usually required in the range below the  $\beta$  phase transition temperature<sup>[25,30]</sup>. Parameter  $n$  determined in the present study changes from a minimum value of 2.9 to a maximum value of 4.6, as shown in the slopes of curves in Fig.4c. This change actually results in a poor prediction of constitutive equation. In order to determine the optimum parameters, the Zener-Hollomon parameter  $Z$ , which correlates the strain rate, deformation

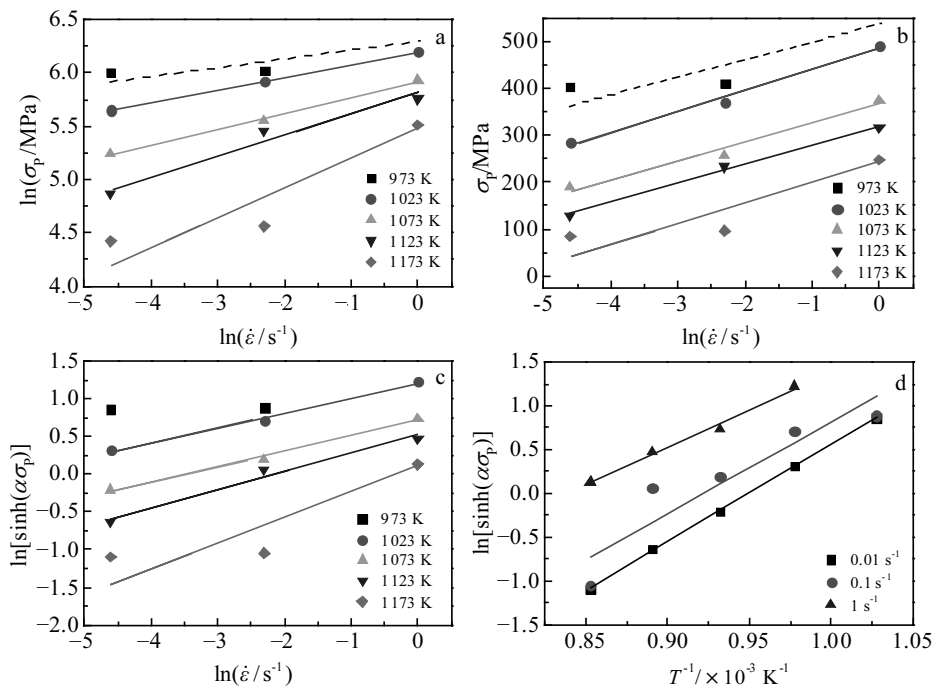


Fig.4 Relationships of  $\ln \sigma_p$  and  $\ln \dot{\epsilon}$  (a),  $\sigma_p$  and  $\ln \dot{\epsilon}$  (b),  $\ln[\sinh(\alpha \sigma_p)]$  and  $\ln \dot{\epsilon}$  (c), and  $\ln[\sinh(\alpha \sigma_p)]$  and  $1/T$  (d)

temperature, and activation energy, is used as follows:

$$Z = \dot{\epsilon} \exp(Q/RT) \tag{7}$$

By combining Eq.(3) and Eq.(7), the logarithm form of  $Z$  can be expressed as follows:

$$\ln Z = \ln[\dot{\epsilon} \exp(Q/RT)] = \ln A + n \ln[\sinh(\alpha\sigma_p)] \tag{8}$$

From Eq.(8) the parameters of  $A$  and  $n$  can be obtained from the linear fitting of  $\ln Z - n \ln[\sinh(\alpha\sigma_p)]$  curves, as shown in Fig.5. The determined parameters of  $A$  and  $n$  from the best fitting of the curves are  $5.32 \times 10^{14}$  and 3.64, respectively. Finally, based on the experimental results, the Arrhenius constitutive equation showing the relationship between peak-state flow behavior and thermal mechanical process parameters can be expressed as follows:

$$\dot{\epsilon} = 5.32 \times 10^{14} [\sinh(0.0044\sigma_p)]^{3.64} \exp(-334\ 758/RT), \tag{9}$$

973 K ≤ T ≤ 1173 K

### 2.3 Temperature sensitivity

Deformation temperature can affect the microstructure evolution of alloy, and further affects the high temperature properties of alloys. Thus, the deformation temperature has a great effect on the hot deformation behavior of alloy. Usually, the microstructure evolution of alloys during deformation can be analyzed based on the relationship between flow stress and deformation temperature according to the irreversible thermodynamics, as expressed as Eq. (10).

$$\sigma = k_1 + k_2 T + k_3 T^2 + k_4 T^3 \tag{10}$$

where  $\sigma$  is the flow stress (MPa),  $T$  is the absolute temperature (K),  $k_1$ ,  $k_2$ ,  $k_3$  and  $k_4$  are constants.

The relationships between true stresses and deformation temperatures under different experimental conditions are shown in Fig.6. It can be seen that, at the strain rates of  $1\text{ s}^{-1}$ , the true stress decreases dramatically with increasing the temperature, indicating that the true stress is strongly sensitive to the temperature at high strain rate. At strain rates of 0.1 and  $0.01\text{ s}^{-1}$ , the true stress decreases relatively gently, which indicates that the softening effect related to deformation temperature under this condition is relatively weak. At a constant temperature, the true stress of the alloy tends to decrease slightly with the increase of the alloy strain. To better understand the effect of temperature on the flow stress, the

modified function of deformation temperature sensitivity ( $\theta$ ) is applied, as expressed as Eq.(11)<sup>[19]</sup>.

$$\theta = \left| \frac{\partial \sigma}{\partial T} \right| = |k_2 + 2k_3 T + 3k_4 T^2| \tag{11}$$

Based on Eq.(11), the 3D maps of the temperature sensitivities under different conditions are plotted, as shown in Fig.7. It can be seen that, at high deformation temperature and low strain rate, the temperature sensitivity generally shows low values. This implies that flow stress is not affected obviously with respect to the change of temperature, but related to the microstructure evolution mechanisms. Thus, the lower  $\theta$  values of alloys mean relatively stable microstructure evolution mechanisms. It also indicates that the whole system inside alloys during hot deformation is easier to enter a balanced state and the corresponding alloy has wider workability range in the low  $\theta$ -value field<sup>[19]</sup>. At high strain rate and low temperature, temperature sensitivity increases significantly, and this may be due to the occurrence of complex microstructure evolution and their interactions, which make the internal system unstable and further lead to distinct softening effect. In the fields either at low temperature with low strain rate or at high temperature with high strain rate, temperature sensitivity of the alloys at early stage of compression (at  $\epsilon=0.1$ ) has relatively high values, implying that hot workability of this field is not good. With

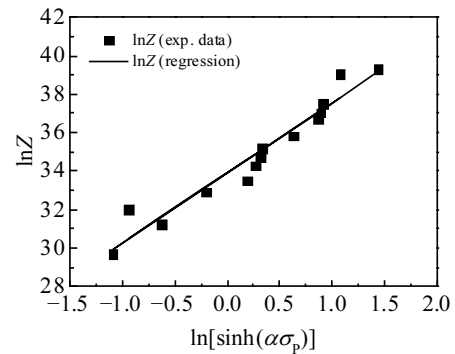


Fig.5 Relationships between Zener-Hollomon parameters  $Z$  and  $\ln[\sinh(\alpha\sigma_p)]$

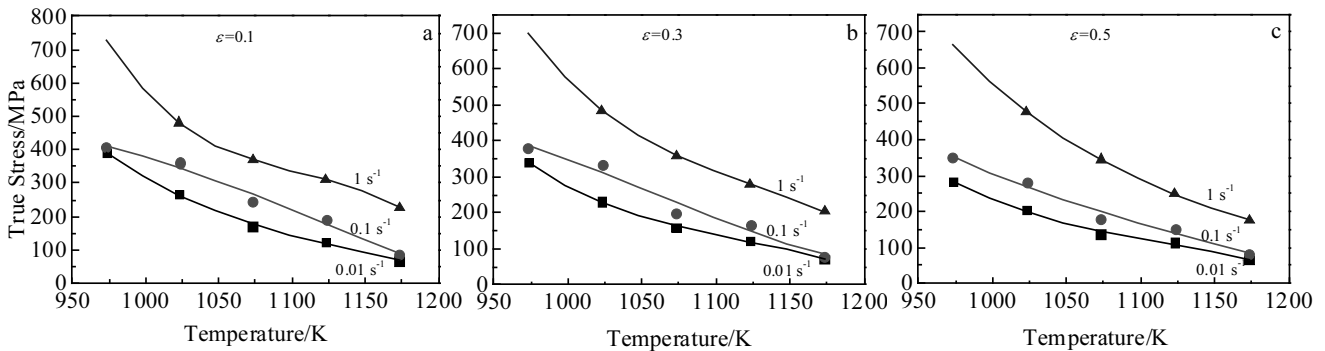


Fig.6 Relationships between true stress and deformation temperature at different strains: (a)  $\epsilon=0.1$ , (b)  $\epsilon=0.3$ , and (c)  $\epsilon=0.5$

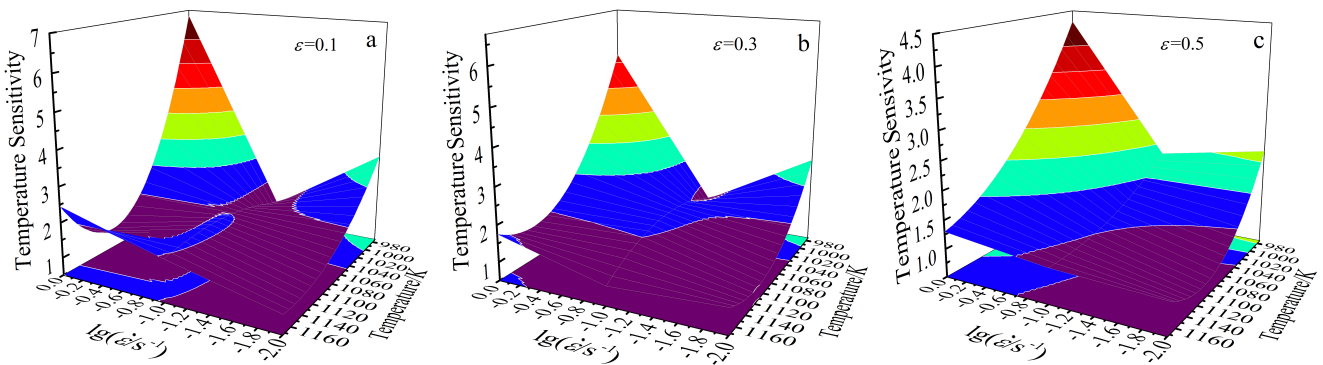


Fig.7 3D maps of the change of temperature sensitivity at different strains: (a)  $\epsilon=0.1$ , (b)  $\epsilon=0.3$ , and (c)  $\epsilon=0.5$

the increase of strain during compression, temperature sensitivity of alloy gradually covers most of experimental conditions except high deformation temperature and low strain rate corner, as shown in Fig.7c.

**2.4 Strain rate sensitivity**

In addition to temperature, another main parameter affecting the hot deformation behavior of the alloy is strain rate. It is known that high strain rate at a fixed temperature will result in high deformation resistance due to strong work hardening. In addition, high strain rate can enhance the temperature by generation of deformation heat, so it may induce the occurrence of softening. Thus, the effect of strain rate on flow stress is quite complicated. According to irreversible thermodynamics, the relationship of true stress and strain rate at a certain temperature and strain can be expressed as Eq.(12).

$$\ln \sigma = a_1 + a_2 \ln \dot{\epsilon} + a_3 (\ln \dot{\epsilon})^2 + a_4 (\ln \dot{\epsilon})^3 \quad (12)$$

where  $\dot{\epsilon}$  is the strain rate,  $a_1$ ,  $a_2$  and  $a_3$  are constants.

The relationships between true stresses and strain rate at different strains and temperatures are shown in Fig.8. It clearly shows that the true stress has an increase tendency with increasing the strain rate. With the increase of strain, the true stress at different deformation temperatures presents a similar increase curve, indicating that the stress state and microstructure evolution have similar behavior. To understand

the effect of strain rate on the hot deformation behavior, the strain rate sensitivity ( $m$ ) is introduced, as expressed as Eq.(13).

$$m = \frac{\partial(\ln \sigma)}{\partial(\ln \dot{\epsilon})} = a_2 + 2a_3 \ln \dot{\epsilon} + 3a_4 (\ln \dot{\epsilon})^2 \quad (13)$$

The strain rate sensitivity is characterized as the plasticity deformation capability of alloys during hot deformation. In general, high strain rate sensitivity is the necessary condition to acquire good plasticity property while negative strain rate sensitivity may reveal the forming of defects inside the materials<sup>[19,31]</sup>. Fig.9 is the contour maps of the strain rate sensitivity of alloy under different strains. It can be seen that the strain rate sensitivity is significantly affected by temperature and strain rate. In Fig.9, the low  $m$ -value appears in the field of low strain rate and high strain rate in the whole temperature range, implying that these domains are not good for plastic deformation. From the macro-appearance of deformed samples shown in Fig.2, either failure sample or most samples with cracks on the surface are in these ranges. The high  $m$ -value mainly appears in the middle range of strain rate in all temperature range. At present study, the determined  $m$ -values vary from  $-0.1$  to  $0.6$  and similar results can be found in other Ti alloys<sup>[19,31]</sup>. In case of strain of  $0.5$ , the maximum  $m$ -value is  $0.54$  and it appears at  $1173$  K and  $0.16$  s<sup>-1</sup>

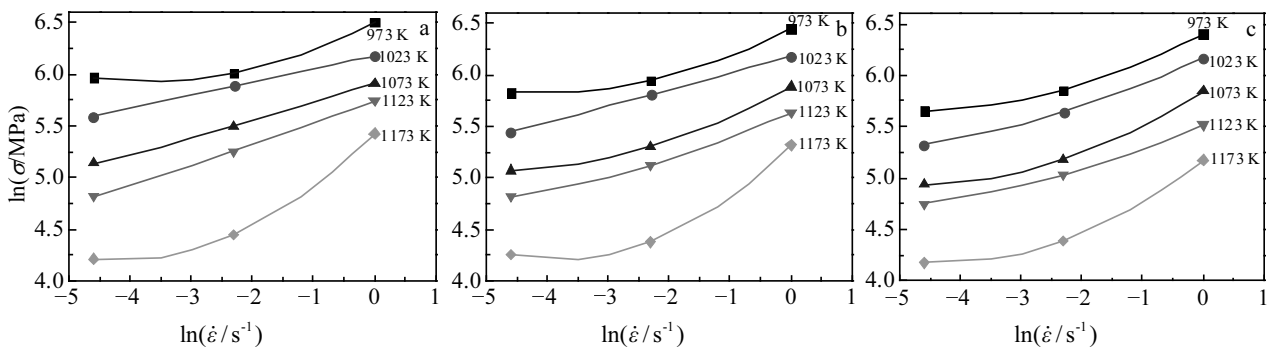


Fig.8 Relationship between true stresses and strain rate at different strains: (a)  $\epsilon=0.1$ , (b)  $\epsilon=0.3$ , and (c)  $\epsilon=0.5$

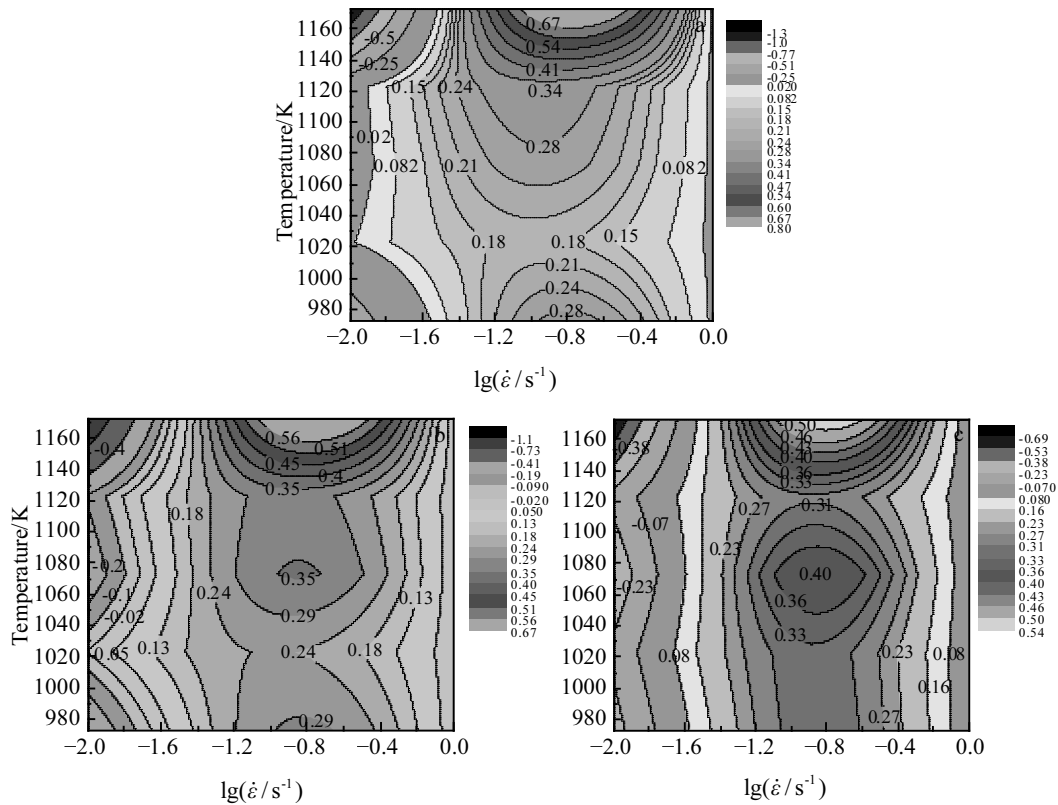


Fig.9 Contour maps of the strain rate sensitivity at strain of 0.1 (a), 0.3 (b), and 0.5 (c)

(or  $\ln \dot{\epsilon} = -0.788$ ), implying that the super plastic deformation is easy to occur in this domain. As shown in the figure, with increasing the strain, the field of negative  $m$ -value expands to center field and the new peak zone of  $m$ -value appears near 1073 K and  $0.14 \text{ s}^{-1}$  (or  $\ln \dot{\epsilon} = -0.85$ ).

## 2.5 Microstructure analysis

Metallographic images taken at center of specimens under different conditions are shown in Fig.10. It can be seen that plate-like or polygonal shape of  $\alpha$  phases with different size are randomly distributed in the samples. The plate-like  $\alpha$  phase with a length of 30–50  $\mu\text{m}$  and a thickness less than 30  $\mu\text{m}$  generally shows deformation perpendicular to compression axis, while the  $\alpha$  phase with relatively large polygonal shape does not show any preferred deformation flow. This can be simply explained by the fact that phases with different size in as-sintered alloys exhibit different deformation resistance during compression. In all the experimental conditions, near globular shape or equiaxed grains with a size less than 20  $\mu\text{m}$  are usually observed near the  $\alpha$  lath boundary, indicating that dynamic recrystallization (DRX) occurs. In addition, as shown in the alloy deformed at 1023 K and  $0.01 \text{ s}^{-1}$ , the sub-grains are observed inside the primary  $\alpha$  grain. This can be explained by the fact that the compression can break up the coarse lamellar grains and facilitate the formation of refined equiaxed microstructures through recrystallization of the  $\alpha$  grains<sup>[5]</sup>.

Another microstructure is characterized by the fine parallel array structure as shown in sample deformed at 973 K/ $0.01 \text{ s}^{-1}$ . This structure can be formed due to local overheating. Due to the poor thermal conductivity of Ti-1100 alloy, the distortion energy caused by deformation cannot be released in the form of heat immediately, which may result in local overheating and the formation of fine parallel structure<sup>[32]</sup>. If this problem is serious, it may cause the flow localization, as shown in sample deformed at 1073 K/ $0.01 \text{ s}^{-1}$  and 1123 K/ $0.1 \text{ s}^{-1}$ .

It is well known that, localized plastic flow, shear deformation or shear band, cracking, etc, which are called flow instability, should be avoided in the hot deformation. In general, macro-cracking, localized plastic flow and shear deformation are easy to form at low temperatures and high strain rates<sup>[19,28,33]</sup>, and micro-cracking is possible to occur at high temperatures and low strain rates<sup>[33-35]</sup>. Fig.11 shows some failure features observed at the center zone of sample. For samples deformed at 973 K/ $0.1 \text{ s}^{-1}$  (Fig.11a) and 1173 K/ $0.01 \text{ s}^{-1}$  (Fig.11d), the shear deformation in near 45° angle to the compression axis is observed, which can certainly affect the stability of alloys during hot deformation. Besides, the cracking is observed in samples deformed at 1023 K/ $0.1 \text{ s}^{-1}$  (Fig.11b) and 973 K/ $0.1 \text{ s}^{-1}$  (Fig.10b<sub>1</sub>). Also, inhomogenous microstructure is observed in the sample deformed at 1073 K/ $0.01 \text{ s}^{-1}$  (Fig.11c). These microstructures are undesirable

and correspond to the flow instability region.

In general, DRX or DRV is the main mechanism of the flow stress softening in hot deformation<sup>[27]</sup>. Usually, DRX occurs more obviously in the sample deformed at lower temperature and lower strain rate<sup>[29]</sup>. In the present study, the DRX is generally observed, as shown in Fig.10, so the DRX is one mechanism of flow stress softening. Moreover, the activation energy ( $Q$ ) determined in present study is much higher than the self-diffusion activation energy of  $\alpha$  phase (150 kJ/mol), implying that softening mechanism is DRX rather than non-diffusion recovery type of DRV<sup>[19,27,31]</sup>. Another possible cause of flow stress softening may be the formation of micro-voids, which can be formed during hot

deformation, especially in the alloys at high strain rate with low temperature range. Fig.12 shows the microstructures of alloys deformed at strain rate of  $1 \text{ s}^{-1}$  with different temperatures. It can be seen that in the sample deformed at 1023 K, lots of micro-voids less than  $5 \mu\text{m}$  are observed at the interface between  $\alpha$  phase and  $\beta$  phase, and the porosity of this micro-voids decreases with increasing the temperature at the same strain rate of  $1 \text{ s}^{-1}$ . In the PM process, these pores can be possibly formed accompanied with serious intergranular micro-cracking due to high stress concentration during hot deformation<sup>[34]</sup>, which thus further cause the reduction of flow stress. Also, the temperature sensitivity curve shown in Fig.7 exhibits the maximum value under this experimental condition, which

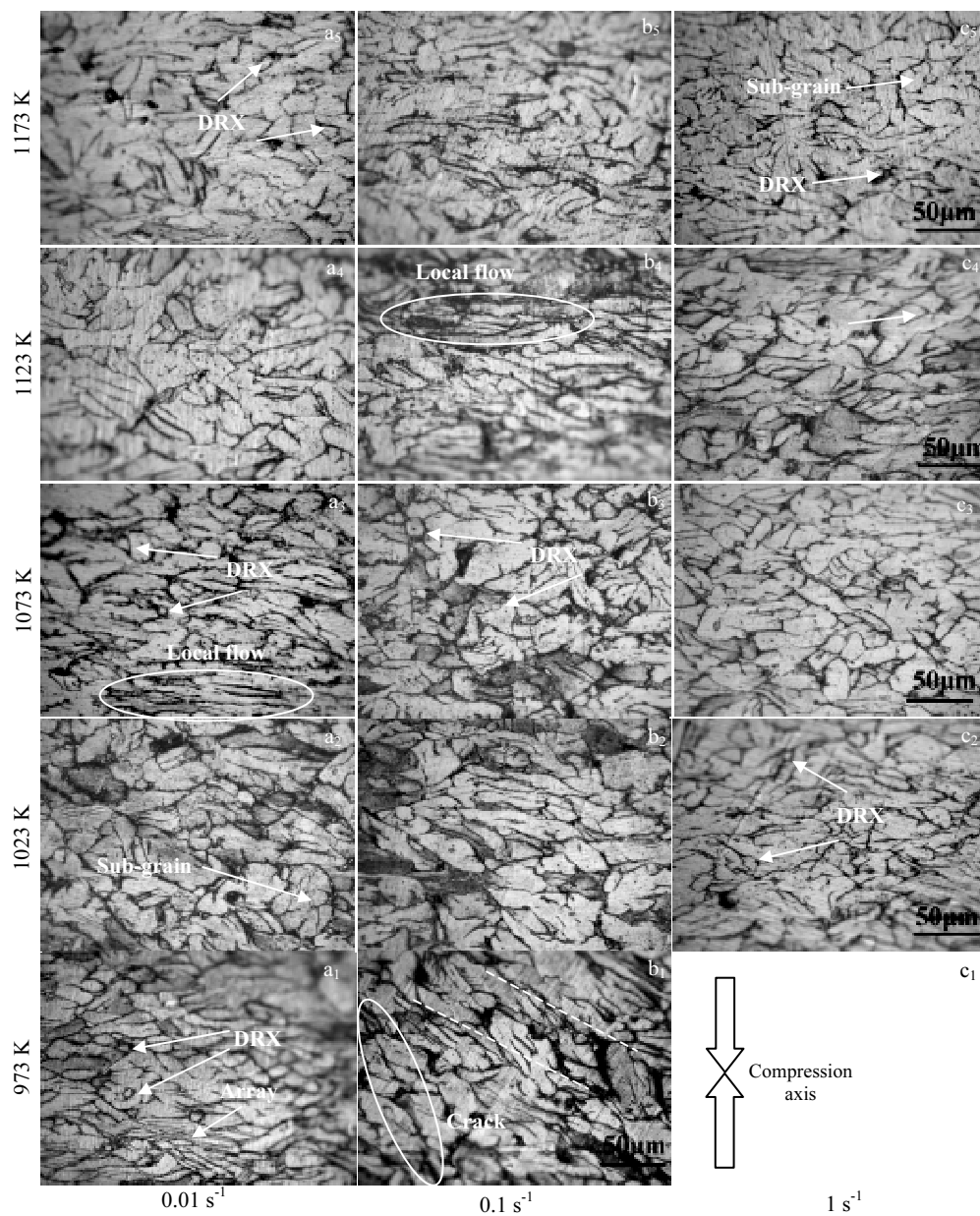


Fig.10 Microstructures of alloy with a strain of 0.5 at different temperatures and strain rates

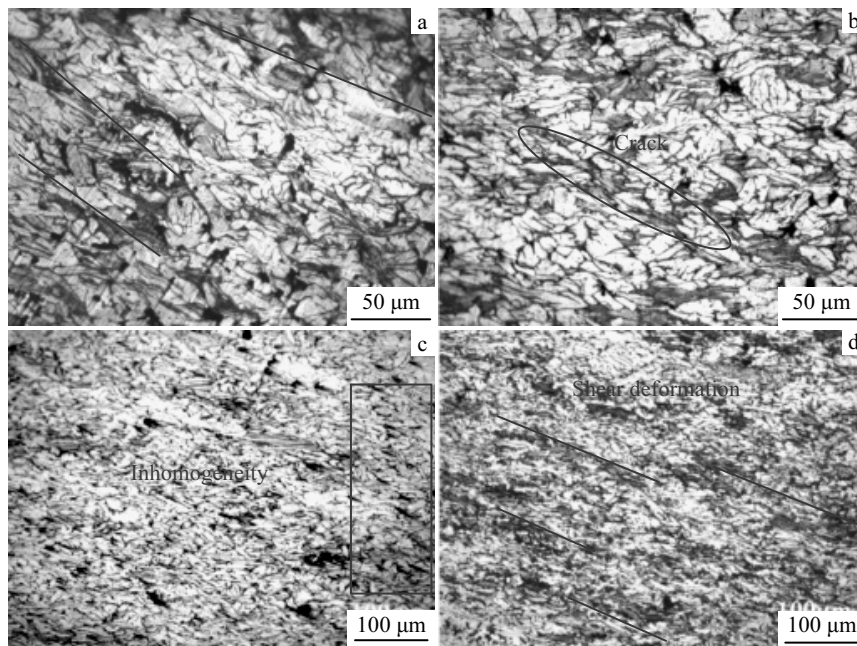


Fig.11 Failure features in center zone of sample compressed under different conditions: (a) 973 K/0.1 s<sup>-1</sup>, (b) 1023 K/0.1 s<sup>-1</sup>, (c) 1073 K/0.01 s<sup>-1</sup>, and (d) 1173 K/0.01 s<sup>-1</sup>

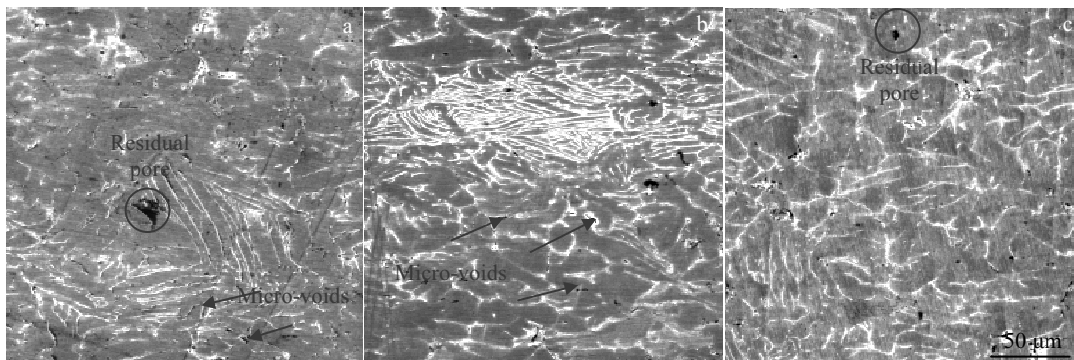
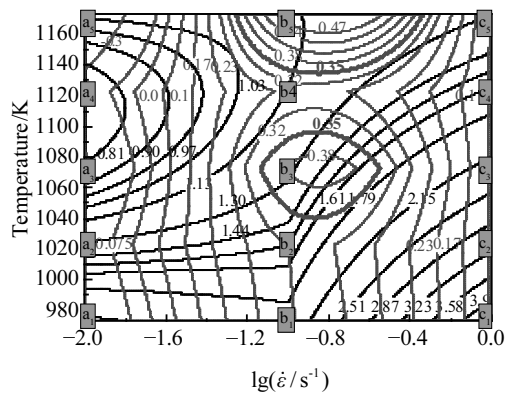


Fig.12 Microstructures of alloys at strain rate of 1 s<sup>-1</sup> under different temperatures: (a) 1023 K, (b) 1073 K, and (c) 1173 K

reveals that severe deformation occurs with high stress concentration. As a consequence, the formation of micro-voids generated in compression process is dominant mechanism of flow softening at low and high strain rates.

To identify the relationship among microstructure evolution, temperature sensitivity and strain rate sensitivity, the stacking contour map consisting of temperature sensitivity ( $\theta$ ) and strain rate sensitivity ( $m$ ) at true strain of 0.5 is plotted, as shown in Fig.13. In the figure, the black line and red line are temperature sensitivity and strain rate sensitivity, respectively, and the green symbols stand for the experimental conditions of present study. In Fig.2, the macro-cracks are generally found in the domains at strain rate of 0.01 and 1 s<sup>-1</sup> at all temperatures, and the corresponding conditions are denoted as a and c series in Fig.13.

From the microstructural analysis discussed in Fig.10 and Fig.11, other instability phenomena such as localized flow (a<sub>3</sub> and b<sub>4</sub>), shear deformation (b<sub>1</sub> and a<sub>5</sub>), micro-crack (b<sub>1</sub> and b<sub>2</sub>), and micro-voids (c<sub>2</sub> and c<sub>3</sub>) are also observed. All these conditions correspond to the instability region, so it should be avoided in hot working process. At strain rate of 0.01 and 1 s<sup>-1</sup>, the corresponding instability domains are located in the region of  $m < 0.1$  and  $\theta < 1.03$  or  $\theta > 1.30$ . Also, at strain rate of 0.1 s<sup>-1</sup>, the flow instability appears at temperature of 973, 1023, and 1123 K, as denoted as b<sub>1</sub>, b<sub>2</sub>, b<sub>4</sub>. The corresponding  $\theta$ -value/ $m$ -value is 1.95/0.312, 1.53/0.318, and 1.13/0.286, respectively. In addition, it can be seen from the microstructure that no any obvious instability is observed at strain rate of 0.1 s<sup>-1</sup> with the temperature 1073 and 1173 K. These stability conditions are



$a_1 \sim a_5 - 0.01 \text{ s}^{-1}$ ,  $b_1 \sim b_5 - 0.1 \text{ s}^{-1}$ ,  $c_1 \sim c_5 - 1 \text{ s}^{-1}$ ;  $a_1 \sim c_1 - 973 \text{ K}$ ,  $a_2 \sim c_2 - 1023 \text{ K}$ ,  $a_3 \sim c_3 - 1073 \text{ K}$ ,  $a_4 \sim c_4 - 1123 \text{ K}$ ,  $a_5 \sim c_5 - 1173 \text{ K}$

Fig.13 Stacking contour map of temperature sensitivity and strain rate sensitivity at the strain of 0.5

very close to the two peak regions of strain rate sensitivity, so the field with  $m$ -value greater than 0.35 indicated in bold red lines may be the optimal condition. As a consequence, it is concluded that the suggested optimal hot working area is mainly in range of 1135 K/0.29  $\text{s}^{-1}$  to 1173 K/0.76  $\text{s}^{-1}$ , and 1040 K/0.33  $\text{s}^{-1}$  to 1096 K/0.6  $\text{s}^{-1}$ .

### 3 Conclusions

1) The hot deformation activation energy value of near- $\alpha$  type Ti-1100 alloy compressed at temperatures of 973~1173 K and strain rates of 0.01, 0.1 and 1  $\text{s}^{-1}$  is determined to be 334.76 kJ/mol. Then, by combining Zener-Hollomon parameter, the Arrhenius constitutive model of this alloy is developed.

2) The temperature sensitivity ( $\theta$ ) and strain rate sensitivity ( $m$ ) can be calculated and the optimal hot working condition is analyzed based on the sensitivity map and microstructure at strain of 0.5. The flow instability mainly occurs at strain rate of 0.01 and 1  $\text{s}^{-1}$  over the whole temperature range of 973~1173 K, where macro-cracking, flow localization, micro-cracking and shear deformation are generally observed. The suggested optimal hot working condition is mainly in range of 1135 K/0.29  $\text{s}^{-1}$  to 1173 K/0.76  $\text{s}^{-1}$ , as well as 1040 K/0.33  $\text{s}^{-1}$  to 1096 K/0.6  $\text{s}^{-1}$ .

3) The dynamic recrystallization is the main mechanism of flow softening at strain rate of 0.1~1  $\text{s}^{-1}$ , while the formation of micro-voids at the interface of  $\beta$  phase and  $\alpha$  grain during compression is the dominant mechanism at 1  $\text{s}^{-1}$  and low temperatures due to high temperature sensitivity.

### References

- Williams J C, Starke E A. *Acta Materialia*[J], 2003, 51(19): 5775
- Bania P J. *JOM*[J], 1988, 40(3): 22
- Fujishiro S, Eylon D, Kishi T. *Metallurgy and Technology of Practical Titanium Alloys*[M]. TMS, 1994
- Hagiwara M, Emura S. *Materials Science & Engineering A*[J], 2003, 352(1): 85
- Fang Z Z, Paramore J D, Sun P et al. *International Materials Reviews*[J], 2018, 63(7):407
- Lütjering G, Williams J C. *Titanium*[M]. Berlin: Springer, 2007
- Zhang H R, Niu H Z, Zang M et al. *Materials Science & Engineering A*[J], 2020, 770: 138 570
- Fang Z Z, Sun P, Wang H. *Advanced Engineering Materials*[J], 2012, 14(6): 383
- Joshi V V, Lavender C, Moxon V et al. *Journal of Materials Engineering and Performance*[J], 2013, 22(4): 995
- Azevedo C R F, Rodrigues D, Neto F B. *Journal of Alloys and Compounds*[J], 2003, 353(1-2): 217
- Ivasishin O M, Eylon D, Bondarchuk V I et al. *Defect and Diffusion Forum*[J], 2008, 277: 177
- Carman A, Zhang L C, Ivasishin O M et al. *Materials Science & Engineering A*[J], 2011, 528(3): 1686
- Ivasishin O M, Savvakina D G. *Key Engineering Materials*[J], 2010, 436: 113
- Wang H T, Lefler M, Fang Z Z et al. *Key Engineering Materials*[J], 2010, 435: 157
- Krishna V G, Prasad Y V R K, Birla N C et al. *Journal of Materials Processing Technology*[J], 1997, 71(3): 377
- Zhou D, Zeng W, Xu J et al. *Advanced Engineering Materials*[J], 2019(21): 180 123 2
- Balasundar I, Raghu T, Kashyap B P. *Materials Science and Engineering A*[J], 2014, 600: 135
- Sellars C M, McTegart W J. *Acta Metallurgica*[J], 1966, 14(9): 1136
- Long S, Xia Y F, Hu J C et al. *Vacuum*[J], 2019, 160: 171
- Lin Y C, Chen X M. *Materials & Design*[J], 2011, 32(4): 1733
- Xia Y F, Long S, Wang T Y et al. *High Temperature Materials and Processes*[J], 2017, 36(7): 657
- Xia F Y, Long S, Zhou Y T et al. *Materials Research*[J], 2016, 19(6): 1449
- Quan G Z, Wen H R, Jia P et al. *International Journal of Precision Engineering and Manufacturing*[J], 2016, 17(2): 171
- Momeni A, Dehghani K. *Materials Science and Engineering A*[J], 2010, 527(21-22): 5467
- Zhu Y, Yang S, Ma L et al. *Iron Steel Vanadium Titanium*[J], 2019, 40(5): 50 (in Chinese)
- Yan J, Pan Q L, Li B et al. *Journal of Alloys and Compounds*[J], 2015, 632: 549
- Liu S F, Li M Q, Luo J et al. *Materials Science and Engineering A*[J], 2014, 589: 15
- Yang J, Wang G, Jiao X et al. *Materials Characterization*[J], 2018, 137: 170
- Yang J, Wang G, Jiao X et al. *Journal of Alloys and Compounds*[J] 2016, 695: 1038
- Liu Q, Hui S, Tong K et al. *Journal of Alloys and Compounds*[J], 2019,787: 527
- Seshacharyulu T, Medeiros S C, Frazier W G et al. *Materials Science and Engineering A* [J], 2000, 284(1-2): 184

- 32 Cui X. *Dissertation for Master[D]*, Harbin: Harbin Institute of Technology, 2008
- 33 Tan L, Li Y, He G et al. *Materials Characterization[J]*, 2019, 147: 340
- 34 Yang C, Liu X, Si J et al. *The Chinese Journal of Nonferrous Metals[J]*, 2015, 25(10): 2707 (in Chinese)
- 35 Shams S A A, Mirdamadi S, Abbasi S M et al. *Metallurgical and Materials Transactions A[J]*, 2017, 48(6): 29

## TiH<sub>2</sub>基粉末冶金近 $\alpha$ 钛合金 Ti-1100 的热变形行为

朴荣勋<sup>1,2</sup>, 杨绍利<sup>1,2</sup>, 朱钰玲<sup>3</sup>, 马 兰<sup>1,2</sup>

(1. 攀枝花学院, 四川 攀枝花 617000)

(2. 四川省钒钛资源综合利用重点实验室, 四川 攀枝花 617000)

(3. 西华大学, 四川 成都 610039)

**摘要:** 通过热压缩试验, 研究了 TiH<sub>2</sub> 基粉末冶金近  $\alpha$  钛合金 Ti-1100 在 973~1173 K 温度范围和 0.01~1.0 s<sup>-1</sup> 应变速率范围内的热变形行为。建立了 Arrhenius 本构方程, 计算出的热形变活化能为 334.76 kJ/mol。通过修改函数计算了温度灵敏度 ( $\theta$ ), 确定了应变率灵敏度 ( $m$ )。根据温度灵敏度、应变率灵敏度和应变为 0.5 时的显微组织分析结果, 对热加工条件进行了分析。结果表明, 在应变率为 0.01 和 1 s<sup>-1</sup> 时, 在整个温度范围内出现了失稳区, 而在 1135 K/0.29 s<sup>-1</sup> 至 1173 K/0.76 s<sup>-1</sup>、1040 K/0.33 s<sup>-1</sup> 至 1096 K/0.6 s<sup>-1</sup> 的范围内获得了最佳的热加工条件。此外, 微观结构分析表明, 在 0.01~0.1 s<sup>-1</sup> 的应变速率条件下发生了动态再结晶 (DRX), 而应变率为 1 s<sup>-1</sup> 时微孔的形成是流动软化的主要机制。

**关键词:** Ti-1100 合金; TiH<sub>2</sub> 基粉末冶金; 热压缩试验; Arrhenius 本构模型; 应变率敏感性; 温度敏感性; 热加工性

---

作者简介: 朴荣勋, 男, 1983 年生, 博士, 攀枝花学院钒钛学院, 四川 攀枝花 617000, 电话: 0812-3372090, E-mail: 940310433@qq.com